Flexure-Induced Structural and Electronic Changes in Polymer Supported Membranes of Length Purified Single-Wall Carbon Nanotubes

*John M. Harris[1], Ganjigunte R. S. Iyer[1], Daneesh O. Simien[2], Jeffrey A. Fagan[3], Ji Yeon Huh[3], Jun Young Chun[3], Steven D. Hudson[3], Jan Obrzut[3], Jack F. Douglas[3], Christopher M. Stafford[3], and Erik K. Hobbie[1]**

[1]Department of Physics, Department of Coatings and Polymeric Materials, North Dakota State University, Fargo, North Dakota 58108

[2]Department of Mechanical and Aerospace Engineering, West Virginia University, Morgantown, West Virginia 26506

[3]Polymers Division, National Institute of Standards and Technology, Gaithersburg Maryland 20899

Thin membranes of length purified single-wall carbon nanotubes (SWCNTs) are uniaxially compressed by depositing them on prestretched polymer substrates. Upon release of the strain, the topography, microstructure and conductivity of the films are characterized using a combination of optical/fluorescence microscopy, light scattering, force microscopy, electron microscopy and impedance spectroscopy. Above a critical surface mass density, films assembled from nanotubes of well-defined length (100 nm to 1000 nm) exhibit a strongly nonlinear mechanical response. The measured strain dependence suggests that the films are softening through an alignment of the SWCNTs normal to the direction of prestrain, which at small strains is also apparent as an anisotropic increase in sheet resistance along the same direction. At higher strains the film conductivities increase, which we attribute to a compression-induced restoration of conductive pathways.

*erik.hobbie@ndsu.edu Tel: 701-231-7049

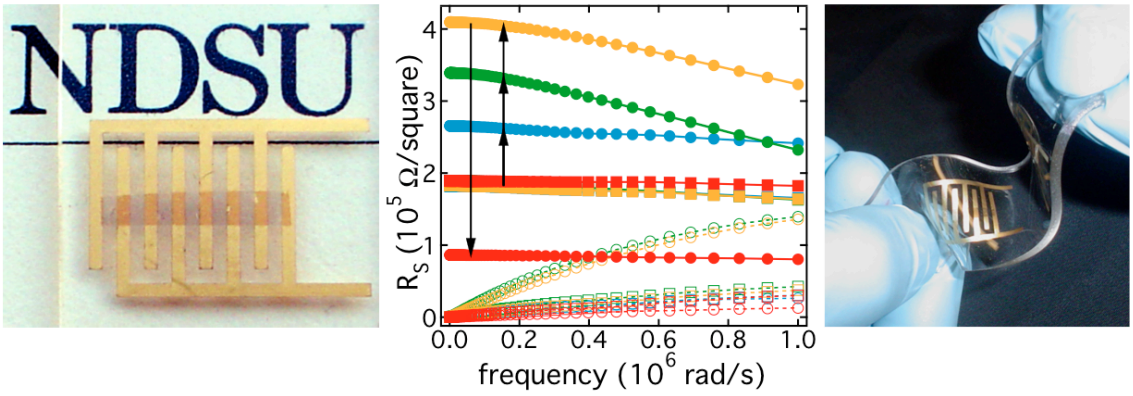

TOC Graphic

INTRODUCTION

In the past two decades, single-wall carbon nanotubes (SWCNTs) have received considerable attention due to their outstanding mechanical, optical and electronic properties, and a vast amount of research has been devoted to the characterization of these attributes[1] and the potential applications they suggest[2]. Thin SWCNT films, in particular, show great promise for applications that require transparent coatings with superior mechanical, electronic and optical qualities[3]. The natural tendency for SWCNTs to form flexible, transparent networks with high electrical conductivity at remarkably low surface coverage is a direct consequence of the magnitude of the typical SWCNT aspect ratio, suggesting that nanotube length is a critical factor in determining the physical properties of such membranes.

The electronic and optical properties of SWCNTs are dictated by their electronic band structure[1], which is specified by the chiral vector (n, m) characterizing the symmetry of rolling a two-dimensional graphene sheet into a hollow tube of diameter a. All existing synthetic techniques therefore produce raw material that contains a distribution of electronic types, ranging from semiconducting to metallic, as well as a broad range of lengths, from 10 nm up to hundreds of micrometers. Since scalable processes for purifying lab-grade quantities of SWCNTs have only recently been formulated[4-6], thin films of these purified materials have just now become readily available for fundamental research, pointing toward a number of promising applications. Thin SWCNT membranes have recently emerged, for example, as a possible replacement for indium tin oxide (ITO) in photovoltaic devices[7] and as potential electrode components in chemical fuel cells[8]. As nanoporous two-dimensional rigid-rod networks, these structures also represent an

intriguing class of mesostructured membrane with poorly understood and potentially complex deformation mechanics[9-12].

Commercial transparent conductive coatings like ITO tend to be brittle, and mechanical flexibility is often cited as a desirable characteristic in the next generation of applications. Given the outstanding intrinsic mechanical properties of SWCNTs, one can anticipate the added benefit that films of purified materials might offer in the area of mechanical performance, beyond the usually quoted optical and electronic benchmarks. The bending mechanics of individual SWCNTs on flexible polymer substrates have recently been investigated by measuring the amplitude and wavelength associated with periodic nanotube buckling under a compressive strain[13]. Applying a continuum-mechanical model to such data yields a nanotube Young's modulus of around 1.3 TPa in reasonable agreement with predictions[14-19]. Analogous mechanical studies of quasi-two dimensional (2D) percolated SWCNT networks are less developed. In one recent study[20], mixed-length and mixed-type SWCNTs were chemically treated to create strong interfacial adhesion on polydimethylsiloxane (PDMS) substrates. Chemical functionalization can have a significantly adverse effect on intrinsic nanotube properties[21], however, despite the improved mechanical properties that chemical grafting can induce.

In this contribution we use a variety of characterization techniques to measure the mechanical and electronic response of thin membranes assembled from unfunctionalized length-purified SWCNTs on polymer substrates, and we correlate the mechanical behavior with changes in the electronic transport properties of the films. Our measurements reveal a material that is remarkably stiff under infinitesimal deformation, but which wrinkles and softens dramatically at finite strains. Correspondingly, this

mechanical softening is initially apparent as an anisotropic decrease in film conductivity, but with a subsequent anisotropic *increase* at sufficiently high strains. We recently[22] modified a theoretical model originally developed by Balberg[23] to link this type of strain softening to an upward shift in percolation threshold triggered by strain-induced nanotube alignment. Here, we extend this analysis to measurements of film conductivity and we demonstrate the critical role of compliance at the electrode-membrane interface, a requirement that relates directly to the relatively small yield strains of the neat SWCNT films in question and puts limits on electrode thickness.

RESULTS AND DISCUSSION

Details related to nanotube purification, membrane production/transfer, and the techniques used to characterize the films can be found in the Methods and Materials section. Surfactant-stabilized aqueous suspensions with mean SWCNT lengths L = (950, 820, 210, and 130) nm were produced using density-gradient ultracentrifugation[24-25]. The optical absorption spectra of the starting suspensions are shown in Fig. 1(a). Although of mixed electronic type, the SWCNTs have a natural enrichment in the (6, 5) semi-conducting species by virtue of the synthetic scheme used to produce the raw materials[26]. The relatively small band-gap leads to a photoluminescence in the near infrared (NIR), which we exploit here to image the membranes with fluorescence microscopy[27]. The thin (10 nm to 100 nm) SWCNT films are mesoporous [Fig. 1(c)] with a mass-fractal structure that can be measured in reciprocal space with small-angle light scattering (SALS); $I(q) \propto q^{-D}$ where q is the scattered wave-vector [Fig. 1(d)]. The fractal dimension D is insensitive to changes in L and surface mass density, c, which is consistent with what has been observed in the high-aspect-ratio limit ($L/a \to \infty$) for the

diffusion-limited cluster aggregation of rod-like colloids[28]. Physically, the influence of primary particle size diminishes once the nanotubes assemble into a network.

The wrinkling pattern that develops upon release of the prestrain reflects the disordered structure of the membranes, as shown in Fig. 2 (a)-(d). In contrast to a pure harmonic, the deformation is hierarchical with an average length scale that decreases strongly with strain that we identify as the wrinkling wavelength. The reciprocal-space structure factor [Fig. 2(e)-(f)] is analogous to that exhibited by several complex materials under strain or flow, including a variety of nanoparticle-polymer networks[29]. The morphology diagram [Fig. 2(g)] shows three different states; unpercolated (Region I, as determined by electrical conductivity), percolated but unwrinkled up to 20 % prestrain (Region II, as determined by electrical conductivity and microscopy), and percolated with wrinkles (Region III). The phase boundaries scale inversely with length as predicted theoretically[22], and the three states can be distinctly resolved with NIR fluorescence microscopy near a membrane edge that has multiple layers [Fig. 2(h)].

The wrinkles seen in optical microscopy contain smaller undulations or folds that can be further resolved with force microscopy [AFM, Fig 3(a) and (b)] and scanning-electron microscopy [SEM, Fig. 3(f)]. Such creases are consistent with good adhesion of the SWCNT membrane to the PDMS; delamination of the film from the substrate leads to large regions of significant relief. At still smaller scales, we can visualize the strain-induced anisotropy directly with transmission electron microscopy [TEM, Fig. 3(c)-(e)], where the most striking contrast comes from SWCNT bundles aligned normal to the prestrain. As detailed below, the film thickness h is a critical parameter in the analysis. We use AFM to measure the mean step height, $\bar{h}$, at the film edge [Fig. 4(a)] and we use

NIR fluorescence microscopy to measure the same step in PL at larger scales [Fig. 4(b)], which provides a consistent measure of SWCNT mass concentration that we use to refine the AFM measurements. As expected, the data suggest a linear relationship between $\bar{h}$ and c [Fig. 4(c)], where the slope is identified as the inverse SWCNT mass density [ρ_s = (0.7 ± 0.3) g/cm^3 for the data shown here]. To obtain an effective "envelope" or maximal thickness h appropriate to a continuum theory, we thus divide $\bar{h}$ by the SWCNT volume fraction in the membranes.

The anisotropy that develops at the microscale is also evident in the structure factor measured with static light scattering, as can be seen by comparing the digital structure factor computed from optical micrographs [Fig. 5(a)] with the measured SALS pattern [Fig. 5(b)]. Projected along the strain direction (x), the scattering peaks coincide [Fig. 5(c)] but the width of the peak normal to the strain direction (y) is much smaller in SALS [Fig. 5(d)]. The peak position provides a measure of the characteristic wrinkling length equivalent to that obtained directly from real space micrographs [Fig. 5(e)]. In contrast, Cartesian projections of the pattern in Fig. 5(a) provide a measure of the coherent dimensions, ξ_x and ξ_y, associated with film topography at optical scales. The correlated spacing of these anisotropic structures gives rise to the scattering peaks, with the peak width providing a stronger measure of shape. The smaller width measured with SALS [Fig. 5(d)] is consistent with the stronger underlying anisotropy revealed by TEM [Fig. 5(g)], which corresponds to SWCNT bundles aligned normal to the prestrain axis (y).

The nonlinear buckling of thin stiff membranes on soft substrates is a long-standing problem in continuum mechanics. In the realm of nanotechnology, this approach has proven useful for determining thin-film elasticity where traditional methods of

measurement are impossible[30]. A common theme is the deposition of a uniform film of relatively high modulus onto a much thicker and softer substrate that has been stretched uniaxially to a specified prestrain ε. In the linear regime, the membrane is modeled as a buckled plate and the substrate as a Hookean solid[31]. Upon release of the prestrain, a homogeneous film of thickness h and modulus E_f develops a sinusoidal wrinkling pattern of wavelength $\lambda_0 = 2\pi h\left(\bar{E}_f / 3\bar{E}_s\right)^{1/3}$ and amplitude $A_0 = h\sqrt{\varepsilon / \varepsilon_c - 1}$ when the prestrain ε exceeds a critical value $\varepsilon_c = \frac{1}{4}\left(3\bar{E}_s / \bar{E}_f\right)^{2/3}$, where $\bar{E}_i = E_i / (1 - \nu_i^2)$ is the plane-strain modulus defined in terms of the Young's modulus E_i and Poisson ratio ν_i of the film ($i = f$) or substrate ($i = s$). To extend this formalism to larger strains, the substrate is modeled as a neo-Hookean solid and λ_0 is scaled by a geometrical prefactor[31] to give $\lambda = \lambda_0(1+\varepsilon)^{-1}(1+\zeta)^{-1/3}$ and $A = A_0 / [\sqrt{1+\varepsilon}\,(1+\zeta)^{1/3}]$ where $\zeta = 5\varepsilon(1+\varepsilon)/32$. The modulus and Poisson ratio of the PDMS substrate are determined independently (Materials and Methods) and a Poisson ratio of 0.3 is assumed for the SWCNT films[32]. Since $E_f \propto (\lambda_0/h)^3$, it is critical to know the film thickness with precision and accuracy.

As shown in Fig. 6(a), the characteristic length scale (λ) determined optically decreases more strongly with prestrain than predicted by the above formalism. The model can, however, explain our observations if we allow the film modulus to be strain dependent, with the expectation that this dependence arises from the rupture of contacts under deformation. The fitted curves [Fig. 6(a)] are thus generalizations of the continuum model to include a strain dependent modulus; $E_f(\varepsilon) = E_{f0}(1+\varepsilon/\varepsilon_0)^{-\delta}$ where E_{f0} is the modulus with respect to infinitesimal deformation and ε_0 is the yield strain. Our data are

consistent with $\delta \approx 2.5$, as indicated in the scaling plot shown in Fig. 6(b). As described previously[22], this expression gives an excellent representation of a more sophisticated model that relates this strain dependence to a shift in percolation threshold triggered by nanotube alignment. The softening of the membranes has the effect of eliminating the increase in wrinkling amplitude with strain predicted by the continuum model when the elastic constant is assumed invariant to deformation. Strain softening in these complex solids is evidently an analog of the power-law shear thinning commonly observed in complex fluids.

The extracted zero-strain modulus E_{f0} [Fig 6(c)] saturates at a value of 320 GPa well below the 1.3 TPa modulus of an individual SWCNT. The results suggest that L only enters the problem through the percolation threshold $c_0(L)$, since data for different lengths all fall on the same curve when plotted against $c/c_0(L)-1$. Although the extrapolated modulus increases dramatically with increasing concentration, this increase is mirrored by a decrease in yield strain that puts limits on any mechanical enhancement. Qualitatively, we can identify a measure of yield-stress, $\varepsilon_0 E_{f0}$, that shows relatively little increase with concentration. This is the typical issue with carbon-nanotube composites, and it is why chemical functionalization is so often employed. It is analogous to the type of yield-stress behavior exhibited by concentrated carbon-nanotube suspensions[33]. Although the film modulus is extrapolated as a fitting parameter and is to some extent approximate, the reported trends are robust. Our future effort will be focused on improving the mechanical behavior of these films using passive approaches, such as SWCNT purification by electronic type and the introduction of an interpenetrating elastomer matrix.

An important and related question is how the softening affects electronic transport. In this regard, it is instructive to consider the evolution from hard to soft substrates, as depicted in Fig. 7. The typical change in film morphology upon release of the prestrain is shown in Fig. 7(a)-(b), where the texture in Fig. 7(a) results from swelling of the PDMS substrate during transfer of the SWCNT film. The electrode geometry is shown in Fig. 7(c). The best transport properties are obtained for SWCNT films deposited on glass [Fig. 7(d)], presumably because the strains associated with substrate swelling/deswelling in PDMS slightly disrupt the nanotube network. Clues into the origin of the softening are provided by the decrease in electrical conductivity normal to the prestrain observed for modest strains, which indicates that conductive pathways are being anisotropically broken by the deformation of the film. This is likely the same breakdown of network junctions responsible for mechanical softening. The connection between this developing anisotropy and the decrease in film stiffness and conductivity follows if we consider that alignment of extended particles reduces the percolation threshold, as recently demonstrated in sheared carbon nanotube melt composites[34] and stretched bulk SWCNT-polymer composites[35]. Here, the orientation results from the strain imposed on the membrane through the combined contraction and Poisson expansion of the substrate[22].

Although the Au electrodes are deposited after release of the prestrain, the fragility of the SWCNT membranes ultimately influences the nature of electrical contact with the electrodes, as shown in Fig. 7(e)-(f). Thicker electrodes [200 nm, Fig. 7(e)] are less compliant to the substrate, which causes the SWCNT films to break at the contacts in response to routine handling associated with characterization. The situation can be substantially improved by using thinner electrodes [100 nm, Fig. 7(f)]. Accounting for

breaks and defects in the films as measured through AFM and optical microscopy, reducing the electrode thickness from 200 nm to 100 nm results in a threefold decrease in sheet resistance.

Finally, the evolution of sheet resistance with strain is examined in Fig. 8. Well into the regime of equilibrium percolation, the conductivity normal to the prestrain initially decreases - as described above - with very little change along the direction of prestrain. Alignment leads to the breaking of network contacts normal to the prestrain, while compression maintains such contacts orthogonal to this. If the decrease is indeed linked to the softening of the membrane, then the two trends should scale accordingly. We previously measured[36] the electrical percolation behavior of unstrained films assembled on filter paper from identical SWCNT fractions, where the conductivity scaled as $\sigma \propto [c/c_0(L)-1]^t$ with $t \simeq 1.4$. Our model of strain softening[22] also gives an expression for the strain-induced increase in percolation threshold; $c_0(\varepsilon) \simeq c_0(1+\varepsilon/\varepsilon_0)^{\delta/\alpha}$ where α is the percolation exponent for elasticity[22] [$E_f \propto (c/c_0-1)^{\alpha}$]. These combine to give $R_s(\varepsilon)/R_s(0) \simeq (1+\varepsilon/\varepsilon_0)^{\delta t/\alpha}$ where R_s is the sheet resistance and there are no free parameters. For small strains, the data do indeed follow this trend [Fig. 8(a)-(c)], but the tendency reverses at strains above 10 % where the conductivity starts to increase. This can also be explained intuitively, since at sufficiently large strains the compression of the membrane will eventually bridge contact between aligned bundles and restore the conductivity normal to the prestrain [Fig. 8(d)].

CONCLUSIONS

Our generalization of a continuum model to films with a strain dependent modulus is successful in capturing essential aspects of wrinkling in strained SWCNT membranes. The hypothesis of network destruction due to nanotube alignment can be independently confirmed through conductivity measurements at small strains, but this trend is eventually overcome by the restoration of electrical contacts through compression. There is even the suggestion of an enhancement in conductivity that we speculate arises from the improved charge transport along the aligned SWCNT bundles once these become sufficiently interconnected. These observations highlight an important distinction between electrical and elastic percolation that is evident in the relative magnitude of the two critical exponents t and α. While the rigidity of the film can continue to improve with additional contacts, this is less true for conductivity. A few good contacts are sufficient for charge transport, and beyond this there is little improvement. Similarly, these contacts do not have to be mechanically rigid. In principle, a single interconnected path is sufficient for charge flow, while many such pathways are required for rigidity.

An immediate implication of these observations is the use of these SWCNT films as electronic strain sensors. To a degree this is already possible and promising. Substantial improvement can still be made, however, through limiting the plastic nature of the structural changes that arise through these types of deformation[22]. The SWCNT bundling that we image here is strongly irreversible, and improving the elastic response of these films will be the emphasis of future research. In the case of transparent conducting SWCNT films, incorporating a polymer into the nanotube network is a promising approach for improving mechanical performance[37,38], but the type of deformation

imposed here is considerably more severe than what is usually considered. Our goal is to make the pristine SWCNT films as robust as possible by the metrics defined here, which will offer a route to conducting polymer nanocomposite films with exceptional optical and mechanical characteristics.

MATERIALS AND METHODS

Materials

SWCNTs grown by the cobalt-molybdenum catalyst (CoMoCat) process were purchased from Southwest Nanotechnologies (S-P95-02 grade, batch NI6-A001). They were dispersed at 1 mg soot/mL in a 2 % by mass sodium deoxycholate (DOC) aqueous solution by tip sonication for 1.5 h in an ice water bath at 1 W/mL applied power. Purification was performed by centrifugation at 21×10^3 *G* for 2 h to pellet the non-SWCNT impurities. Density layers were formed from varied concentrations of iodixanol-deoxycholate solutions. Separation was performed in a SW-32 rotor using a Beckman Coulter L80 XP ultracentrifuge at 1445 rad/s for 70 h. Individual fractions were collected in 1.5 mL increments. From these, we selected four fractions, with *L* as determined by AFM and TEM and further verified by the intensity of the resonant absorption peak at 984 nm. The combined relative uncertainty in *L* is 10 % with a standard deviation of 20 %. Length fractions were dialyzed against 0.8 % DOC solution to remove the remaining iodixanol and reduce the surfactant concentration.

Nanotubes were deposited on cellulose-ester filter paper of diameter 47 mm and mean pore size 0.05 μm using vacuum filtration[39]. A mixture of isopropanol and deionized water (1:4 by volume) was used to condition the filter and DI water was used to rinse away surfactant. The surface density was controlled by quantifying the volume of

fractionated suspension (of known concentration) using a micropipette and diluting the suspension with DI water to 2 mL. The samples were dried at 50 °C for 24 h under a nitrogen atmosphere and the surface density for percolation determined through impedance spectroscopy as a function of surface coverage[36]. The mass of SWCNT per unit area of the membrane (*c*) was determined from the amount of SWCNT deposited onto a known area of filter paper. The concentration of SWCNT in the parent solution is determined from the nonresonant (baseline) optical absorption at 775 nm. The extinction coefficient obtained (2.1 mL/mm/mg) is close to values in the literature and is consistent with the measured absorbance at 775 nm in the sonicated, pre-centrifuged suspension (for which the mass fraction is precisely known). The validity of the spectroscopic approach was confirmed for both length polydisperse and length fractionated suspensions by weighing the amount of SWCNT deposited on filter paper membranes.

Substrates (PDMS, Sylgard 184; Dow Corning Co.) were prepared by hand-mixing an oligomeric base and curing agent (10:1 by mass). The mixture was left at room temperature overnight to allow trapped air bubbles to escape and cured at 75 °C for 2 h. The cured PDMS substrates (thickness ≈ 1.5 mm) were cut into 25 mm × 75 mm strips. Each strain measurement corresponds to one PDMS substrate, with up to four SWCNT membranes on a substrate. The strain was imposed on a strain gauge equipped with a micrometer[40] and the rate of release was kept constant to control for variations in morphology with rate. The zero-strain state was defined in one of two ways. For imaging measurements that could be performed on samples mounted in the gauge (optical microscopy), a small (*ca.* 5 %) reference strain was imposed prior to applying the prestrain and depositing the SWCNTs. The prestrain was then precisely defined by

releasing the gauge back to this reference. This approach assumes the PDMS remains approximately linear-elastic up to 30 % strain, which we measured to be the case. Equivalently, transmission light microscopy of the mounted PDMS oriented at 45^{o} with respect to two crossed polarizers was used to monitor the transmitted intensity as a function of micrometer setting, and the stress-optical rule was then invoked to define the zero-strain position. The elastic modulus of the PDMS was measured to be 1.8 MPa using a standard uniaxial tensile tester (Texture Analyzer, Model TA.XT2i; Texture Technologies) and a Poisson ratio of 0.48 was assumed. Using values other than 0.3 for the Poisson ratio of the SWCNT membranes had very little effect on the trends reported.

Small sections of each SWCNT membrane were deposited on PDMS (strained and unstrained), glass and quartz by back dissolving the filter paper with acetone. The SWCNTs have a natural affinity for interfaces, even when they are stable by most metrics for colloidal suspensions[39]. Substrates of PDMS completely immersed in acetone for 24 h slightly swell[42], but the films here were exposed over a limited region of surface area for less than 30 min total. Residual strain from solvent swelling effects was estimated to be less than 2 % and was orientated normal to the direction of the applied prestrain [Fig. 7(a)]. Consequently, any wrinkling due to swelling was relatively weak, was oriented at 90° to the direction of the wrinkling front of interest, and was minimally discernable after release of the prestrain. The wrinkling wavelength is an ensemble average of values for several different regions of the same membrane obtained optically and with AFM.

Methods

Optical absorption spectroscopy was performed in transmission mode on a Perkin Elmer Lambda 950 UV-Vis-NIR spectrophotometer at (185 to 1880) nm. The incident light was circularly polarized and the instrument was corrected for both the dark current and background spectra. The reference beam was left unobstructed during the measurement with the subtraction of the appropriate reference sample performed during data reduction. Absorption spectra were recorded at 1 nm increments, with an instrument integration time of 0.2 s per increment, using a (1, 2, or 10) mm quartz cuvette, depending upon the extinction for a particular sample. Fluorescence characterization was performed on a JY-Horiba nanolog-3 spectrofluorometer with a liquid-nitrogen cooled InGaAs detector. Emission spectra were corrected for source spectral distribution, detector spectral response, and for the absorbance of the filter used to restrict the scattered excitation light from the NIR monochromotors and detector. Excitation wavelength was scanned in 5 nm increments using a 450 W xenon lamp through a 10 nm slit with emission collected at 90° in either (1, 2 or 4) nm increments through a 10 nm slit.

The wrinkling morphology was characterized with SALS, reflection optical microscopy, AFM, SEM, and TEM. Static light scattering measurements were performed with a 30 mW He-Ne directed through the strained film, with the scattered light imaged on a screen equipped with a beam stop using a thermoelectrically cooled CCD. Optical microscopy was performed in both reflection and epi-illumination NIR fluorescence (with a liquid-nitrogen cooled InGaAs CCD) using 10-50x objectives. The local topography of the wrinkled membranes was measured with AFM in tapping mode. Scanning electron microscopy (SEM) measurements were performed using standard protocols on untreated membranes. Samples for TEM were prepared by shadowing the

membranes with platinum/carbon (Pt/C) and then evaporating a thin film of carbon onto the shadowed membrane. A film of polyacrylic acid (PAA) was then cast onto this surface. After drying at 55 °C overnight, the PAA was removed, causing the membrane and evaporated carbon to detach from the PDMS. The PAA was dissolved in water and the floating SWCNT membranes retrieved on copper grids. The thin Pt/C coating provided only weak image contrast, the primary features arising from local variations in the SWCNT density.

To measure sheet resistance, an interdigitated electrode pattern was sputtered on to the SWCNT membranes through a shadow mask. A 10 nm base layer of chromium was used to improve electrode contact and adhesion, followed by a 100-200 nm layer of gold. Electrical measurements were analyzed in terms of complex impedance, yielding the impedance magnitude ($|Z^*|$) and the corresponding phase angle (ϑ) as a function of frequency. The impedance was measured as a function of frequency between 10^{-2} kHz and 10^{3} kHz using a four-terminal fixture attached to an Agilent 4294A precision impedance analyzer, calibrated with a standard extension adapter to short, load, and open standards. Measurements were also performed on an Agilent B 1500A semiconductor device analyzer in both 2 and 4-probe geometries, calibrated against 1.01 μF capacitor. The impedance was normalized to sheet resistance using the geometry of the electrode pattern and membrane corrected to account for breaks in the film. The combined relative experimental uncertainty is 4 % and the experimental uncertainty of the phase angle measurements is ± 0.5°. For measurements on strained films, electrodes were deposited on two separate membranes prepared on the same PDMS substrate. One pair was oriented

to measure film conductivity along the direction of prestrain and the other was rotated 90^{o} with respect to this.

Note: Certain equipment, instruments, or materials are identified in this paper in order to adequately specify the experimental details. Such identification does not imply recommendation by the National Institute of Standards and Technology nor does it imply the materials are necessarily the best available for the purpose.

ACKNOWLEDGEMENTS

EKH would like to acknowledge the support of the NSF through CMMI-0969155 (JH) and the DOE through DE-FG36-08GO88160 (SI). The authors would also like to thank Thuy Chastek, Benjamin Forsythe, and Steven Ruckdashel for assistance with the measurements.

REFERENCES

1. Saito, R.; Dresselhaus, G.; Dresselhaus, M. S., *Physical Properties of Carbon Nanotubes* (Imperial College Press, 1999).

2. Baughman, R. H.; Zakhidov, A. A.; de Heer, W. A., "Carbon nanotubes-the route toward applications", *Science* **2002**, 297, 787-792.

3. Cao, Q.; Rogers, J. A., "Ultrathin films of single-walled carbon nanotubes for electronics and sensors: A review of fundamental and applied aspects", *Adv. Mater.* **2008**, 21, 29-53.

4. Hersam, M. C., "Progress towards monodisperse single-walled carbon nanotubes", *Nature Nanotechnol.* **2008**, 3, 387-394.

5. Tu, X.; Manohar, S.; Jagota, A.; Zheng, M., "DNA sequence motifs for structure-specific recognition and separation of carbon nanotubes", *Nature* **2009**, 460, 250-253.

6. Fagan, J. A.; Becker, M. L.; Chun, J.; Hobbie, E. K., "Length fractionation of carbon nanotubes using centrifugation", *Adv. Mater.* **2008**, 20, 1609-1613.

7. Hu, L.; Hecht, D. S.; Grüner, G., "Infrared transparent carbon nanotube thin films", *Appl. Phys. Lett.* **2009**, 94, 081103.

8. Landi, B. J.; Ganter, M. J.; Cress, C. D.; DiLeo, R. A.; Raffaelle, R. P., "Carbon nanotubes for lithium ion batteries", *Energy Environ. Sci.* **2009**, 2, 638-654.

9. Song, L.; Ci, L.; Lv, L.; Zhou, Z.; Yan, X.; Liu, D.; Yuan, H.; Gao, Y.; Wang, J.; Liu, L.; Zhao, X.; Zhang, Z.; Dou, X.; Zhou, W.; Wang, G.; Wang, C.; Xie, S.; "Direct synthesis of a macroscale single-walled carbon nanotube non-woven material", *Adv. Mater.* **2004**, 16, 1529-1534.

10. Baughman, R. H.; Cui, C.; Zakhidov, A. A.; Iqbal, Z.; Barisci, J. N.; Spinks, G. M.; Wallace, G. G.; Mazzoldi, A.; De Rossi, D.; Rinzler, A. G.; Jaschinski, O.; Roth, S.; Kertesz, M., "Carbon nanotube actuators", *Science* **1999**, 284 1340-1344.

11. Zhang, X. F.; Sreekumar, T. V.; Liu, T.; Kumar, S., "Properties and structure of nitric acid oxidized single wall carbon nanotube films", *J. Phys. Chem. B* **2004**, 108, 16435-16440.

12. Pham, G. T.; Park, Y.-B.; Wang, S.; Liang, Z.; Wang, B.; Zhang, C.; Funchess, P.; Kramer, L., "Mechanical and electrical properties of polycarbonate nanotube buckypaper composite sheets" *Nanotechnology* **2008**, 19, 325705.

13. Khang, D.-Y.; Xiao, J.; Kocabas, C.; MacLaren, S.; Banks, T.; Jiang, H.; Huang, Y. Y.; Rogers, J. A., "Molecular scale buckling mechanics in individual aligned single-wall carbon nanotubes on elastomeric substrates", *Nano Lett.* **2008**, 8, 124-130.

14. Li, C.; Chou, T.-W., "Modeling of elastic buckling of carbon nanotubes by molecular structural mechanics approach", *Mechanics of Materials* **2004**, 36, 1047-1055.

15. Yakobson, B. I.; Brabec, C. J.; Bernholc, J., *Phys. Rev. Lett.* **1996**, 76, 2511-2514.

16. Yu, M.-F.; Files, B. S.; Arepalli, S.; Ruoff, R. S.; "Tensile loading of ropes of single wall carbon nanotubes and their mechanical properties" *Phys. Rev. Lett.* **2000**, 84, 5552-5555.

17. Srivastava, D.; Menon, M.; Cho, K., *Phys. Rev. Lett.* **1999**, 83, 2973-2976.

18. Kis, A.; Zettl, A., "Nanomechanics of carbon nanotubes", *Phil. Trans. R. Soc.* A **2008**, 366, 1591-1611.

19. Wei, C.; Cho, K.; Srivastava, D., "Tensile strength of carbon nanotubes under realistic temperature and strain rate", *Phys. Rev. B* **2003**, 67, 115407.

20. Yu, C.; Masarapu, C.; Rong, J.; Wei, B.; Jiang, H., "Stretchable supercapacitors based on buckled single-walled carbon-nanotube macrofilms", *Adv. Mater.* **2009**, 47, 4793-4797.

21. Wang, C.; Cao, Q.; Ozel, T.; Gaur, A.; Rogers, J. A.; Shim, M., "Electronically selective chemical functionalization of carbon nanotubes: Correlation between Raman spectral and electrical responses", *J. Am. Chem. Soc.* **2005**, 127, 11460-11468.

22. Hobbie, E. K.; Simien, D. O.; Fagan, J. A.; Huh, J. Y.; Chung, J. Y.; Hudson, S. D.; Obrzut, J; Douglas, J. F.; Stafford, C. M., "Wrinkling and strain softening in single-wall carbon nanotube membranes", *Phys. Rev. Lett.* **2010**, 104, 125505.

23. Balberg, I.; Anderson, C. H.; Alexander, S.; Wagner, N., "Excluded volume and its relation to the onset of percolation", *Phys Rev B* **1984**, 30, 3933-3943.

24. Fagan, J. A.; Becker, M. L.; Chun, J.; Hobbie, E. K., "Length fractionation of carbon nanotubes using centrifugation", *Adv. Mater* **2008**, 20, 1609-1613.

25. Fagan, J. A.; Becker, M. L.; Chun, J.; Nie, P.; Bauer, B. J.; Simpson, J. R.; Hight Walker, A. R.; Hobbie, E. K., "Centrifugal length separation of carbon nanotubes", *Langmuir* **2008**, 24, 13880-13889.

26. Resasco, D. E.; Alvarez, W. E.; Pompeo, F.; Balzano, L.; Herrera, J. E.; Kitiyanan, B.; Borgna, A., "A scalable process for production of single-walled carbon nanotubes (SWNTs) by catalytic disproportionation of CO on a solid catalyst", *Journal of Nanoparticle Research* **2002**, 4, 131-136.

27. Hobbie, E. K.; Fagan, J. A.; Becker, M. L.; Hudson, S. D.; Fakhri, N.; Pasquali, M. "Self-Assembly of ordered nanowires in biological suspensions of single-wall carbon nanotubes" *ACS Nano* **2009**, 3, 189-196.

28. Mohraz, A.; Moler, D. B.; Ziff, R. M.; Solomon, M. J.; "Effect of monomer geometry on the fractal structure of colloidal rod aggregates", *Phys. Rev. Lett.* **2004**, 92,155503.

29. Lin-Gibson, S.; Schmidt, G.; Kim, H.; Han, C. C.; Hobbie, E. K., "Shear-induced mesostructure in nanoplatelet-polymer networks", *J. Chem. Phys.* **2003**, 119, 8080-8084.

30. Stafford, C. M.; Harrison, C.; Beers, K. L.; Karim, A.; Amis, E. J.; Vanlandingham, M. R.; Kim, H. C.; Volksen, W.; Miller, R. D.; Simonyi, E. E., "A buckling-based metrology for measuring the elastic moduli of polymeric thin films", *Nat. Mater.* **2004**, 3, 545-550.

31. Jiang, H.; Khang, D.-Y.; Song, J.; Sun, Y.; Huang, Y.; Rogers, J. A., "Finite deformation mechanics in buckled thin films on compliant supports", *Proc. Natl. Acad. Sci.* **2007**, 104, 15607-15612.

32. Hall, L. J.; Coluci, V. R.; Galvão, D. S.; Kozlov, M. E.; Zhang, M.; Dantas, S. O.; Baughman, R. H., "Sign change of Poisson's ratio for carbon nanotube sheets", *Science* **2009**, 320, 504-507.

33. Hobbie, E. K.; Fry, D. J., "Rheology of concentrated carbon nanotube suspensions", *J. Chem. Phys.* **2007**, 126, 124907.

34. Obrzut, J.; Douglas, J. F.; Kharchenko, S. B.; Migler, K. B., "Shear-induced conductor-insulator transition in melt-mixed polypropylene-carbon nanotube dispersions", *Phys. Rev. B* **2007**, 76, 195420.

35. White, S. I.; DiDonna, B. A.; Mu, M.; Lubensky, T. C.; Winey, K. I., "Simulations and electrical conductivity of percolated networks of finite rods with various degrees of axial alignment", *Phys. Rev. B* **2009**, 79, 024301.

36. Simien, D.; Fagan, J. A.; Luo, W.; Douglas, J. F.; Migler, K.; Obrzut, J., "Influence of nanotube length on the optical and conductivity properties of thin single-wall carbon nanotube networks", *ACS Nano* **2008**, 2, 1879-1884.

37. De, S.; Lyons, P. E.; Sorrel, S.; Doherty, E. M.; King, P. J.; Blau, W. J.; Nirmalraj, P. N.; Boland, J. J.; Scardaci, V.; Joimel, J. et al. "Transparent, flexible, and highly conductive thin films based on polymer-nanotube composites", *ACS Nano* **2009**, 3, 714-720.

38. Hu, L.; Hecht, D. S.; Grüner, G., *Chem. Rev.* **2010**, 110, 5790-5844.

39. Wu, Z. C.; Chen, Z. H.; Du, X.; Logan, J. M.; Sippel, J.; Nikolou, M.; Kamaras, K.; Reynolds, J. R.; Tanner, D. B.; Hebard, A. F.; et al. "Transparent, conductive carbon nanotube films", *Science* **2004**, 305, 1273-1276.

40. Stafford, C. M.; Guo, S.; Harrison, C.; Chiang, M. Y. M., "Combinatorial and high-throughput measurements of the modulus of thin polymer films", *Rev. Sci. Instrum.* **2005**, 76, 062207.

41. Hobbie, E. K.; Bauer, B. J.; Stephens, J.; Becker, M. L.; McGuiggan, P.; Hudson, S. D.; Wang, H., "Colloidal particles coated and stabilized by DNA-wrapped carbon nanotubes", *Langmuir* **2005**, 21, 10284-10287.

42. Lee, J. N.; Park, C.; Whitesides, G. M., "Solvent compatibility of poly(dimethylsiloxane)-based microfluidic devices", *Anal. Chem.* **2003**, 75, 6544-6554.

Figure Captions

Figure 1 - (a) Optical absorption spectra of the four different length fractions. (b) Typical near-infrared (NIR) fluorescence profile in the plane of emission and excitation (L = 950 nm). (c) Scanning-electron microscopy (SEM) image of the porous SWCNT assembly in a dry membrane (L = 820 nm, c = 0.02 μg cm^{-2}, scale = 200 nm). (d) Small-angle light scattering profiles from unstrained dried membranes (L = 130 nm, c = 3.5 μg/cm^2; L = 210 nm, c = 1.7 μg/cm^2; L = 820 nm, c = 0.3 μg/cm^2) deposited on quartz, where the solid curve is a power law-fit to $q^{-1.72}$.

Figure 2 - Reflection optical micrographs of SWCNT membrane wrinkling (L = 130 nm, c = 3.5 μg/cm^2) at prestrains of (a) 2.5 %, (b) 5 %, (c) 10 % and (d) 20 %. The scale bar is 5 μm. (e) Reflection optical micrographs of wrinkling (L = 130 nm, c = 3.5 μg/cm^2) at a prestrain of 2.5 % (scale = 20 μm) and (f) the corresponding numerical power spectrum from the FFT (scale = 0.63 μm^{-1}). (g) State diagram for wrinkling in the plane of c and L. The lower solid line is a fit of the connectivity percolation threshold to inverse aspect ratio and the upper dashed line is the wrinkling threshold. The blue symbols denote membranes that remain flat up to 20 % prestrain and the green symbols denote membrane wrinkling by 2 % prestrain, where the light green markers show a mixed-length (unsorted) response. (h) NIR fluorescent micrograph (L = 130 nm, prestrain = 5 %) showing percolated, unwrinkled membranes (upper right, lower left) and the increase in wrinkling wavelength with thickness.

Figure 3 - AFM images of the wrinkling topography for (a) L = 130 nm, c = 3.5 μg/cm^2 and a prestrain of 5 %, and (b) L = 130 nm, c = 3.5 μg/cm^2 and a prestrain of 2.5 %,

where the scale in each image is 5 μm. (c)-(e) TEM images of wrinkled membranes (L = 130 nm, c = 3.5 μg/cm^2 and a prestrain of 20 %) at progressively smaller length scales, with scale bars of (c) 5 μm, (d) 2 μm, and (e) 150 nm. (f) SEM image reveals the complex topography of wrinkling at smaller length scales (L = 130 nm, c = 3.5 μg/cm^2, prestrain = 5 %, scale bar = 2 μm).

Figure 4 - (a) Typical step-height profile (film thickness) measured with AFM and (b) measured with NIR fluorescence. (c) Mean membrane thickness as a function of surface concentration showing linear behavior for different SWCNT lengths.

Figure 5 - (a) Digital structure factor from an ensemble of optical micrographs and (b) the corresponding light-scattering pattern (10 % prestrain, L = 130 nm, c = 2.9 μg cm^{-2}, scale = 3 μm^{-1}). The compression of the two symmetric lobes along the y-axis, normal to the direction of prestrain suggests anisotropic bundling normal to the direction of prestrain. (c) Projected structure along the strain [horizontal dashed lines in (a) and (b)] with Gaussian fits and (d) projected structure normal to the strain [vertical dashed lines in (a) and (b)] with Gaussian fits. (e) Comparison of wrinkling wavelength determined in real space and reciprocal space. (f) Coherence lengths along and normal to the direction of strain. (e) Anisotropic bundling revealed by TEM (scale = 200 nm).

Figure 6 - (a) Wavelength of the dominant wrinkling mode [legend shown in (b)], where the curves are fits assuming strain softening and the black dashed curve is the elastic nonlinear response. (b) Scaling plot of the softening in the elastic modulus of the film, where the black curve is the empirical power-law expression. (a) Film modulus (circles)

and yield strain (stars) as a function of reduced percolation depth for SWCNT lengths of 130 nm (cross), 210 nm (dot), 820 nm (open), and 950 nm (hatch).

Figure 7 - (a) Region of a membrane (L = 130 nm, c = 3.5 μg/cm^2) before the release of a 5 % prestrain and (b) the same region after release. (c) Electrode configuration used to measure the sheet resistance of the strained membranes, where the dashed white boundary delineates the SWCNT membrane. (d) Complex sheet resistance as a function of frequency for the membrane depicted in (a) and (b) deposited on glass, on unstrained PDMS, and on PDMS after the release of a 5 % prestrain. (e) Fractured gold (left) – SWCNT (right) interface (L = 950 nm, c = 1 μg cm^{-2}, 2.5 % prestrain). The electrode is 200 nm thick (25 μm scale). (f) A nearly intact gold-SWCNT interface for a piece of the same membrane at 15 % prestrain with a 100 nm thick electrode (25 μm scale).

Figure 8 - (a) Complex sheet resistance (real part - solid; imaginary part – open/dashed) as a function of frequency measured parallel (squares) and perpendicular (circles) to the direction of prestrain at 2.5 % (blue), 5 % (green), 10 % (orange) and 20 % (red) strain. Data correspond to L = 950 nm and c = 1 μg cm^{-2}. (b) Sheet resistance for the same sample as a function of strain normal to (blue) and along (red) the axis of prestrain. The black curve is the anticipated strain response based on the softening deduced from wrinkling and the measured percolation conductivity exponent. (c) The same data displayed as reduced sheet resistant as a function of reduced strain on a log-log scale. (d) Anisotropy in the sheet resistance as a function of strain. The inset shows a cartoon showing the effect of strain on electrical connectivity in the membranes.

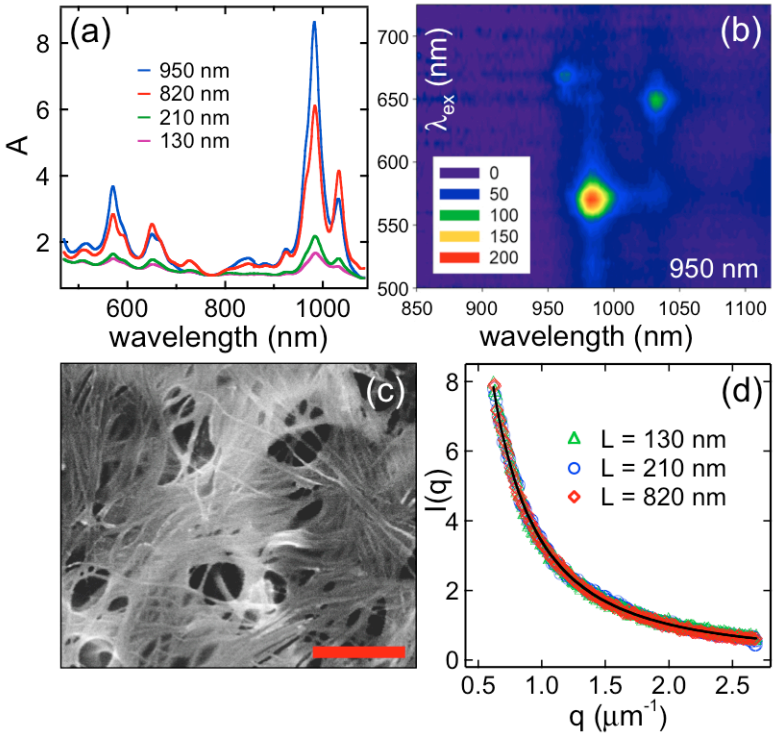
(a)
950 nm
820 nm
210 nm
130 nm
A
wavelength (nm)
(b)
λex (nm)
0
50
100
150
200
950 nm
wavelength (nm)
(c)
(d)
L = 130 nm
L = 210 nm
L = 820 nm
I(q)
q (μm-1)

Figure 1

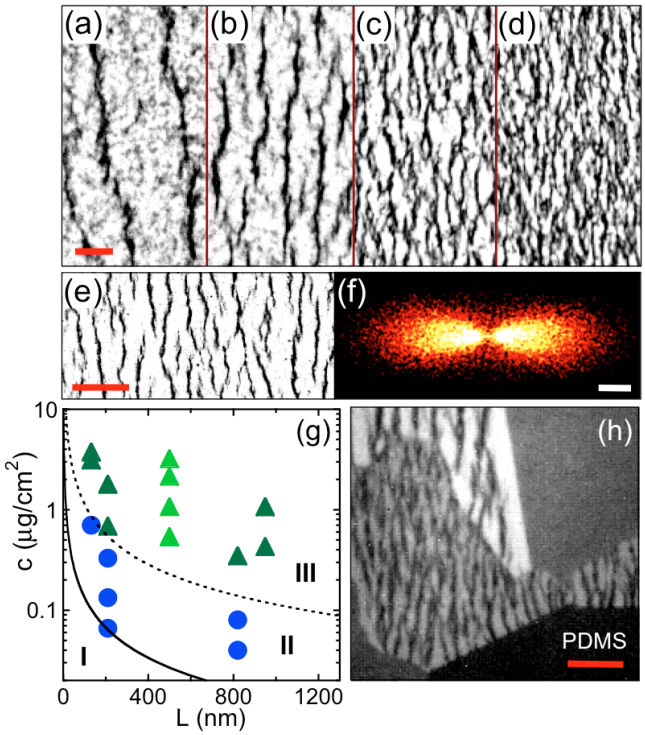

Figure 2

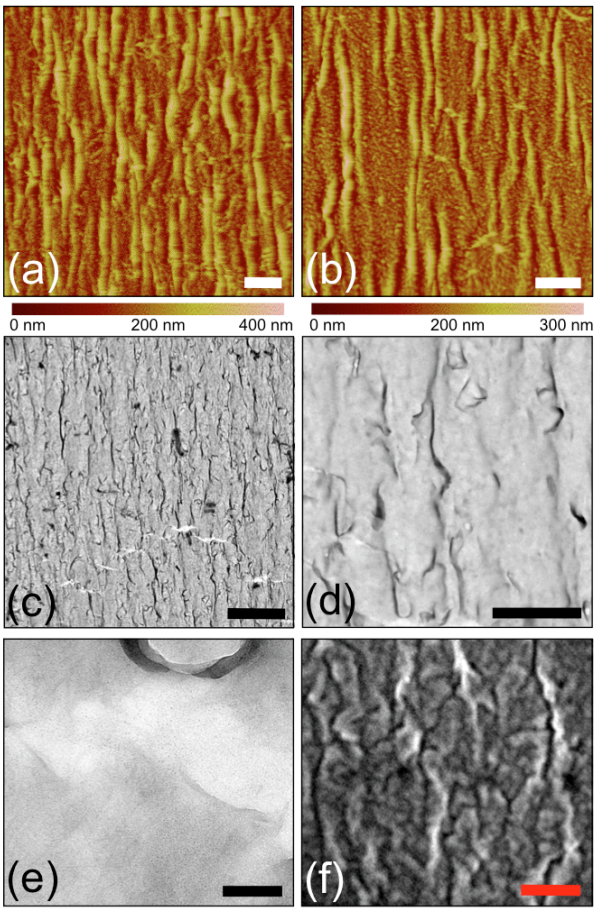

Figure 3

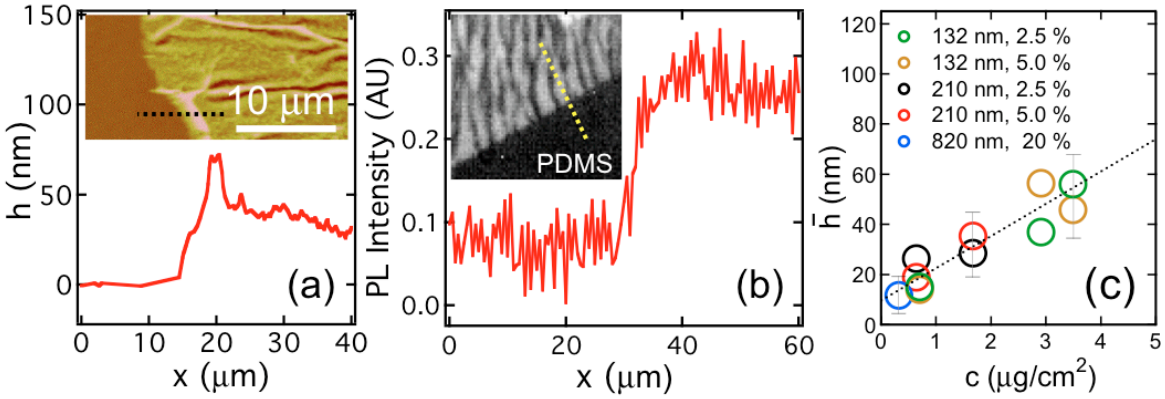
h (nm)
150
100
50
0
10 µm
(a)
0
10
20
30
40
x (µm)
PL Intensity (AU)
0.3
0.2
0.1
0.0
PDMS
(b)
0
20
40
60
x (µm)
$\bar{h}$ (nm)
120
100
80
60
40
20
0
132 nm, 2.5 %
132 nm, 5.0 %
210 nm, 2.5 %
210 nm, 5.0 %
820 nm, 20 %
(c)
0
1
2
3
4
5
c (µg/cm^2)

Figure 4

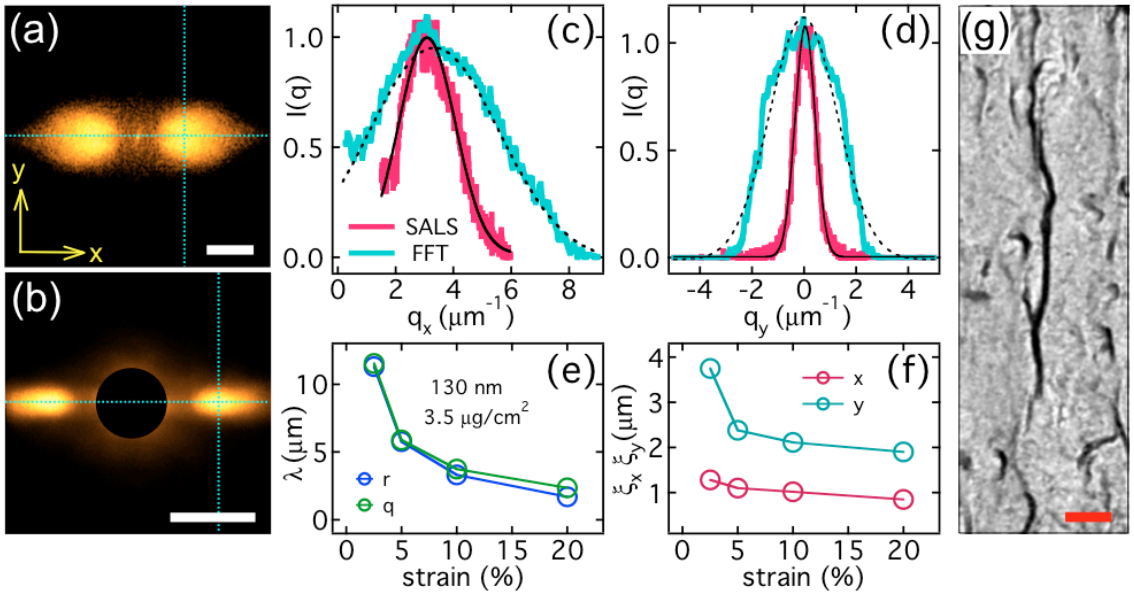
(a)
y
x
(b)
(c)
I(q)
1.0
0.5
0.0
SALS
FFT
0 2 4 6 8
q_x (μm^{-1})
(d)
I(q)
1.0
0.5
0.0
-4 -2 0 2 4
q_y (μm^{-1})
(g)
(e)
λ (μm)
10
5
0
130 nm
3.5 μg/cm^2
r
q
0 5 10 15 20
strain (%)
(f)
ξ_x ξ_y (μm)
4
3
2
1
x
y
0 5 10 15 20
strain (%)

Figure 5

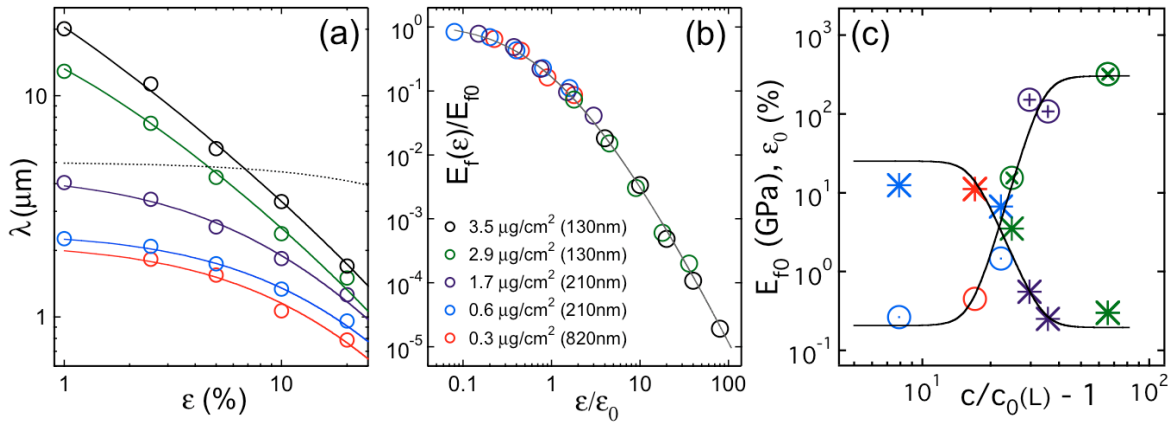
(a)
λ (μm)
ε (%)
(b)
$E_f(\varepsilon)/E_{f0}$
ε/ε0
3.5 μg/cm² (130nm)
2.9 μg/cm² (130nm)
1.7 μg/cm² (210nm)
0.6 μg/cm² (210nm)
0.3 μg/cm² (820nm)
(c)
E_{f0} (GPa), ε_0 (%)
c/c0(L) - 1

Figure 6

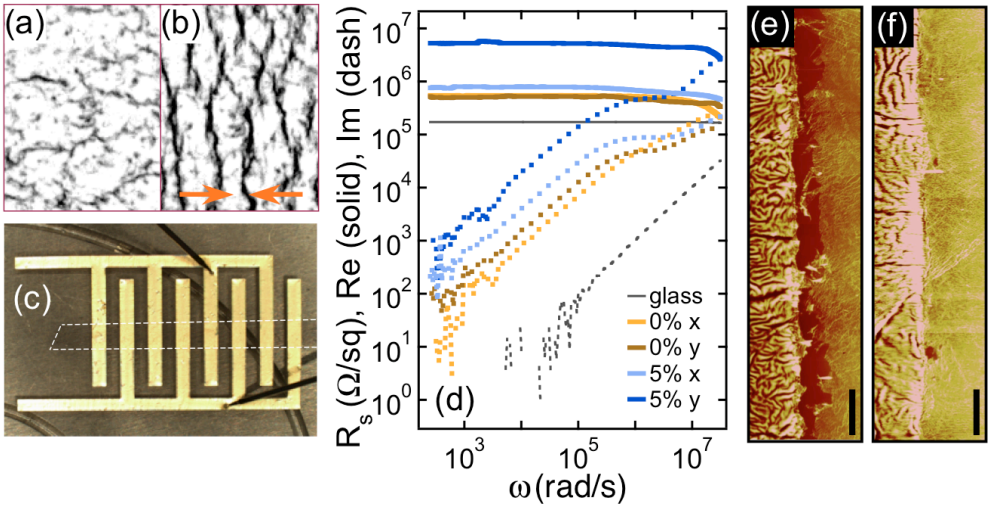
(a)
(b)
(c)
(d)
(e)
(f)
R_s (Ω/sq), Re (solid), Im (dash)
10^0
10^1
10^2
10^3
10^4
10^5
10^6
10^7
10^3
10^5
10^7
ω (rad/s)
glass
0% x
0% y
5% x
5% y

Figure 7

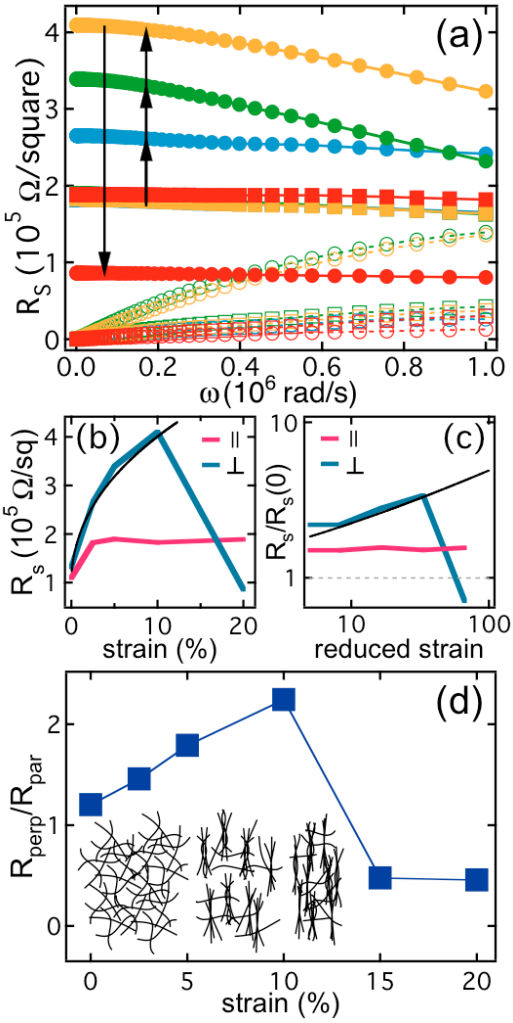
(a)
R_S (10^5 Ω/square)
ω(10^6 rad/s)
(b)
∥
⊥
R_s (10^5 Ω/sq)
strain (%)
(c)
$R_s/R_s(0)$
reduced strain
(d)
R_{perp}/R_{par}
strain (%)

Figure 8